The KPC-Log: A new method for measuring the permeability of a non-cylindrical tight sample

Sandra Profice[1,*] , *Romain* De Loubens[1], *Diego* Potenzoni[2], *Philippe* Chehade[3], *Benjamin* Nicot[1], and *Roland* Lenormand[4]

[1]TOTAL CSTJF, Avenue Larribau, 64018 Pau Cedex, France
[2]PAN AMERICAN ENERGY, Avenida Leandro Nicéforo Alem 1180 (1001), Argentina Buenos Aires, Argentina
[3]ENSG, 2 rue du Doyen Marcel Roubault, 54518 Vandœuvre-lès-Nancy, France
[4]CYDAREX, 31 avenue Gabriel Péri, 92500 Rueil-Malmaison, France

Abstract. When shale cores or core plugs are fractured, the most direct solution to characterize permeability consists in crushing the rock and performing a Gas Research Institute (GRI) test. Yet, crushing efficiency is questionable when observing microfractures in some particles. Moreover, the recorded pressure response is short, the particles being small. If the experimental artefacts at early times are substantial, the interpretation provides erroneous results. Lastly, the sample geometry is systematically simplified but the effect generated on the estimated permeability has never been addressed rigorously. This paper focuses on the KPC-Log, an innovative method for measuring permeability (K) on centimetric pieces (P) of core (C). Reliable values of absolute permeability (k_{abs}) and Klinkenberg coefficient (b) are obtained by interpreting improved GRI tests with a numerical model using as input a 3D image of the sample surface. By studying pieces of rock having variable shapes, we highlighted that simplifying the geometry impacts more b than k_{abs}. This means that the error on the apparent permeability (k_{app}) increases when the mean pore pressure decreases. Furthermore, we confirmed that not elongated cuttings or crushed rock particles can be assimilated to uniform spheres. With the emergence of micro-coring bits, the KPC-Log offers a new way to build a log of permeability.

1. Introduction

Characterizing shales can be a real challenge since these rocks are often laminated and hence brittle [1]. They tend to break easily at the interface between two layers. Cores fracture during tripping from the reservoir to the surface and core plugs, during sampling, cleaning or drying. The CT-scans of Figure 1 were acquired on heavily fractured cores from Vaca Muerta shale formation in Argentina.
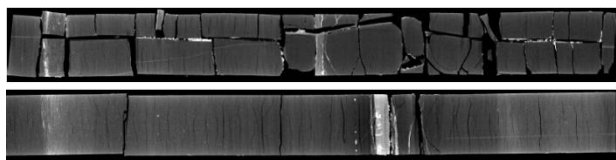

Fig. 1. CT-scans of highly fractured cores from the Argentinian Vaca Muerta shale formation

When dealing with samples having unusual shapes or sizes, the number of methods available in the industry for determining permeability is limited. The most immediate solution would be to crush the sample and perform a Gas Research Institute (GRI) test. Developed in the early 90s by Luffel *et al.* [2] for crushed rocks or drill cuttings, the GRI method consists in exciting the particles with a gas pressure pulse and interpreting the response related to the

gas flow in the pore network to derive the permeability. The test is nothing more than a pycnometry test. Most of the commercial laboratories are currently equipped with the original GRI device, sketched in Figure 2. They tend to prefer particles of a few millimetres while Luffel *et al.* opted for submillimetric particles (0.50 to 0.84 mm).
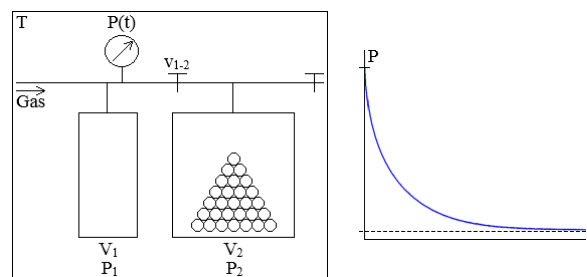

Fig. 2. GRI or pycnometry device and recorded pressure signal

The sample is introduced in a chamber of volume V_2 which is connected to a chamber of volume V_1 by means of a valve v_{1-2}. Initially, the valve v_{1-2} is closed and both the sample pore volume and the dead (or empty) volume in the chamber V_2 are at the pressure P_2 (generally equal to the atmospheric pressure). To start with, the chamber V_1 is pressurized at a pressure P_1 higher than the pressure P_2. At time t=0, the valve v_{1-2} is opened and the recording

---

of the pressure transient P(t) is triggered simultaneously. The system is kept at a constant temperature T either by regulating the laboratory temperature or by placing it in a temperature-controlled oven.

Egermann *et al.* [3] proposed in 2003 a variant of the GRI technique, called Darcylog. At the beginning of the test, the chamber containing the rock particles is flushed with helium and filled afterwards with a viscous oil. The oil spontaneously imbibes in the particles, expelling the helium. At residual helium saturation, the oil pressure is gradually increased from atmospheric pressure to 10 bar so that the oil penetrates in the particles by compressing the trapped gas ganglia. The permeability is obtained by interpreting the oil pressure and injected oil volume data recorded over time with a numerical model. Egermann *et al.*'s Darcylog paved the way for two new variants of the GRI method: Carles *et al.*'s Darcygas [4] and Lenormand *et al.*'s Pulse Decay Open Surface (PDOS) [5], invented in 2007 and 2010 respectively. Both techniques rely on a device with only one chamber whose initial volume can be modified in a very short time by moving a piston. The air filling the dead volume surrounding the sample in the chamber is compressed in a Darcygas test to engender a pressure decay and expanded in a PDOS test to produce a pressure build-up. Interpretation is based on a numerical model for both types of test. The Darcylog, Darcygas and PDOS methods were designed to be applicable on either millimetric particles (1 to 5 mm) or a small cylinder with a diameter of 1 cm and a length of 1.5 cm. The Darcygas and the PDOS are dedicated to tight and unconventional rocks. These two methods and the Darcylog, appropriate for tight and conventional rocks, are complementary.

In addition to the PDOS, Lenormand *et al.* presented in 2010 several methods specific to small cylinders only. The authors undertook steady-state and Pulse Decay tests with gas on plugs whose diameters were close to 0.5 cm and lengths close to 1 cm. Each plug was either inserted in a silicone tube or confined in a Hassler microcell. The inlet pressure did not exceed 100 mbar with the silicone tube, to prevent any gas leak between the sample and the tube. Besides, they took a method introduced for cuttings in the late 90s and they adapted it to plugs with diameters of about 1 cm and lengths varying from 0.2 to 0.5 cm. In their method, called Darcypress, the sample is embedded in a resin disc whose faces are polished until the material shows on the surface, so that the gas can flow through it. After preparation, the disc is placed between the plates of a press to be subjected to a vertical stress. Steady-state or Pulse Decay tests can be conducted and interpreted with the standard analytical or numerical models existing for cylinders. The permeabilities measurable by Darcypress vary in a large range, going from 0.1 nD to a few darcies.

Lastly, the literature provides examples of techniques in which a rather big cylinder undergoes a test similar to a GRI test. Plug diameters and lengths range from 2.5 to 5 cm. In canister degassing tests, studied by Cui *et al.* [6] in 2009 and Zhao *et al.* [7] in 2019, the plug degasses at constant temperature, in a canister at lower and constant pressure. Cui *et al.* derived two analytical expressions for permeability, a first one true at early times and a second one true at late times. The authors used them to interpret the desorbed gas cumulative volume data recorded over time. Zhao *et al.* went further in the modeling process by including anisotropy. The analytical solution, true at any time, enables the computation of horizontal and vertical permeabilities from the gas flow rate data recorded over time. In a paper published 2 years before, Hannon Jr. [8] dealt with anisotropy quantification too by interpretation of data collected during a GRI-type test. His method, the Full-Immersion Pressure-Pulse Decay (FIPPD), relies on the generation of a pressure pulse on the plug surface, by depressurizing a first chamber in the second one holding the sample. The horizontal and vertical permeabilities are obtained by matching the pressure decay simulated from a numerical model with the experimental one. In another version of the FIPPD test, the plug is wrapped in a mesh sleeve before being confined in a core holder. The pulse is emitted at one sample end but the gas flows through its whole surface because of the permeable membrane. The test at the center of the Modified Gas Expansion (MGE) technique, imagined by Peng and Loucks [9] in 2016, is similar, except that the gas invades the medium through its top end only since no mesh sleeve is used. An average permeability is estimated by interpreting the late times of the recorded pressure decay with an analytical solution.

In the majority of the methods previously described, the sample is unconfined [2 -7]. Confining small samples at realistic overburden pressures is not an easy task. This is problematic as low-permeability media are particularly sensitive to stress [10]. Small sample representativity is another important problem. For heterogeneous rocks, the sample size significantly impacts the permeability. When comparing the permeabilities found for a granodiorite by 24 laboratories, David *et al.* [11] noticed that dispersion in the results increased for decreasing plug lengths. Their explanation was that the volumes of the short plugs were potentially below the Elementary Representative Volume (REV), the selected granodiorite having centimetre-sized mineralogical heterogeneities. Permeability variation in Peng and Loucks' work was more related to plug radius variation. The studied rocks were laminated shales. The heterogeneities encompassed in the plugs changed when increasing the radius since sampling was done parallel to bedding. The debate about the place of microfractures in sample representativity and the best manner to deal with a fractured sample is still open in the literature. Luffel *et al.*'s principal argument to defend the GRI method is that microfractures result from coring and thus, must be fully eliminated by rock crushing. Sinha *et al.* [12] were more inclined to keep the plug intact and confine it, given that determining undoubtedly if microfractures are natural or artificial is complicated. Natural microfractures acting as preferential pathways for the gas in the reservoir must be preserved when measuring the permeability. In the case where microfractures are deemed to be artificial, opting for plug confinement is an insufficient solution for Peng and Loucks, these microfractures remaining open even at high confining pressures. Plug crushing is inadequate too for Tinni *et al.* [13] who spotted microfractures in micro-computed tomography images of crushed shale particles

having sizes of 3.5 mm and 0.7 mm. Comisky *et al.* [14] evidenced from mercury injection capillary pressure tests that such microfractures can be crushing-induced and not coring-induced. Profice and Lenormand [15] highlighted it too by analyzing scanning electron microscopy images taken before and after crushing. Several authors attribute another negative effect to rock crushing. Cui *et al.*, Tinni *et al.* and Peng and Loucks proved that the mean particle size decrease leads to a permeability decrease. They did not explain this behavior by a continuous elimination of microfractures. They related it to a gradual damaging of the material pore structure when crushing finer and finer. Cui *et al.* and Peng and Loucks based their reflection on models correlating permeability and pore radius. Tinni *et al.* compared the pore throat size distributions of several samples composed of smaller and smaller particles. Last but not least, crushing makes difficult sample modeling, the particles having variable shapes and sizes distributed in a range depending on the preparation procedure [15]. Though Luffel *et al.* represented the sample as a pack of identical cylinders, most of the authors who focused later on the GRI technique and its derivatives assimilated it to a pack of identical spheres [3 - 6, 9, 13, 15]. The fact that such assumptions can impact the permeability if the true geometry substantially deviates from the simplified one was evoked by Civan [16] but not demonstrated. Suarez-Rivera *et al.* [17] simulated the pressure signal expected from a GRI test for multiple packs of identical particles, the aspect ratio changing from one pack to the other. The simulations revealed that the signal remains close to that corresponding to a pack of spheres while the aspect ratio is low, *i.e.* while the particles are not excessively oblate. To the best of our knowledge, no author has ever deeply examined the errors induced on the estimated properties by the sample geometry simplification.

2. KPC-Log method

TOTAL purchased in 2014 a robot equipped with a laser, which enables the sample surface mapping in 3D and the sample bulk volume computation from the reconstructed surface. The goal was to abandon mercury immersion for bulk volume measurement owing to all problems caused by mercury to health and environment. Very few papers of the petroleum literature refer to this type of device [9], which remains infrequent for bulk volume estimation.

Fig. 3. Laser robot

The sample shape and dimensions must be such that the whole surface can be correctly scanned by the laser. The tiniest samples on which we successfully tested our robot had dimensions hardly reaching a few millimetres. The 3D map of the sample surface is a point cloud image in which any point is located by spatial coordinates. The point cloud is closed by executing a numerical algorithm and the bulk volume is deduced from the 3D envelope.

When facing massive plug breaking during our many studies of cores from Vaca Muerta formation, we had the idea to generate a 3D mesh from the point cloud to make the interpretation of a GRI-type test possible for a piece of rock with a non-geometrical form. Our new technique for determining the permeability of a sample having any shape is named KPC-Log, K referring to "permeability" and PC to "Piece of Core". It offers an innovative way to build a log of permeability, considering the existence of the Micro-Coring Bit (MCB) which provides centimetric micro-cores while drilling [18]. The MCB was proposed by TOTAL and Diamant Drilling Services in 2008. The photos of Figure 4 show the MCB and one of the micro-cores obtained during the first test done with the MCB in an interbedded shale and sandstone formation.

Fig. 4. MCB and one of the micro-cores collected while drilling an interbedded shale and sandstone formation [18]

Cutting the sample of Figure 4 to give it a cylindrical shape would be perhaps possible but likely tricky. In the photo of Figure 5 can be observed pieces of broken core whose forms depart much from the common geometrical ones: sphere, cylinder and disc. Taking plugs from such irregularly shaped fragments of a few centimetres would be too difficult.

Fig. 5. Pieces from a broken shale core having irregular forms and too small sizes to be plugged

With the KPC-Log method, there is no need to crush the sample anymore when its geometry cannot be easily defined or modified. The potential problem of bias in the permeability related to sample modelling disappears, the sample shape being accurately captured. Coring-induced

microfractures are not eliminated but crushing the piece of rock to destroy them seems to be even less satisfactory than keeping it intact. As mentioned before in Section 1, crushing could produce new microfractures and alter the sample representativity by harming its pore structure. In addition, crushing reduces the interval of permeabilities measurable with a GRI-type test. The pressure response duration decreases when the sample exchange area with the gas around increases and its characteristic penetration depth decreases [15]. Therefore, crushing is particularly detrimental for relatively high-permeability media whose responses are already short without crushing, as the even shorter responses after crushing can be inappropriate for interpretation. Instantaneous responses are obviously not reliable. This is also the case for responses hidden by the pressure relaxation caused by the thermal effects created when opening the valve between the two chambers [15]. In the reference [19], Lenormand and Profice describe an innovative solution to reduce these effects. Furthermore, they formulate recommendations about the device design and the experimental procedure. All these improvements brought to the GRI method optimize the estimation of the absolute (or intrinsic) permeability and the Klinkenberg coefficient from several tests on the crushed sample. The authors called Darcyshale their new GRI-type technique. The KPC-Log encompasses the innovations at the origin of the Darcyshale, in addition to the sample form capture innovation. The impacts on the estimated properties that are still uncontrolled with the KPC-Log are those due to the absence of confining stress, rock anisotropy and rock fracturing.

3. Experimental device

The KPC-Log device, schematically drawn in Figure 6, is a bigger version of the device presented in the reference [19] for the analysis of crushed samples or drill cuttings. These devices are comparable to the pycnometry or GRI device of Figure 1 but the operating procedure followed to use them is different from the standard GRI procedure. The sample, piece of rock or rock particles, is introduced in the chamber V_1, chamber pressurized at the beginning of the test. This means that both the sample pore volume V_p and the dead volume in the chamber V_1 are initially at an identical pressure P_1 higher than the pressure P_2 in the chamber V_2, P_2 being equal to the atmospheric pressure. Pressure recording is triggered a few seconds before the time t=0 at which the valve v_{1-2} is opened, to capture the pressure P_1. The system temperature is stabilized at T by regulating the laboratory temperature.
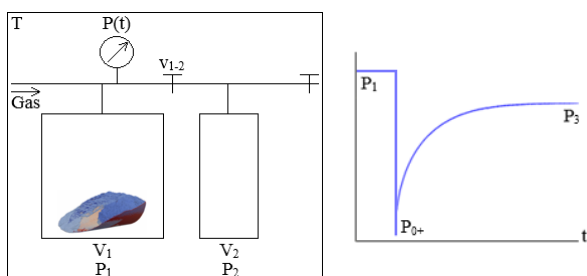

Fig. 6. KPC-Log device and recorded pressure signal

As illustrated through the pressure signal P(t) plotted in Figure 6, the test comprises three successive phases. In the first phase, the chamber V_1 is at pressure balance and the recorded pressure is equal to P_1. In the second phase starting at t=0+ (just after opening the valve v_{1-2}), the gas in the dead volume surrounding the sample expands from the chamber V_1 to the chamber V_2. The pressure decline from P_1 to P_{0+} is assumed to be instantaneous. Moreover, the pressure in the porous medium is supposed to be still equal to P_1 at t=0+. In the third phase, the rock expels its gas until the whole system equilibrates at the pressure P_3. Consequently, the pressure transient interpreted to derive the permeability is a pressure build-up and not a pressure decay as in the majority of the GRI-type methods.

The porosity ϕ can be computed from two equations. Each of them arises from a material balance between two states: initial and final states for Equation (1), initial and transitional states for Equation (2). While initial state and first phase coincide, the transitional state is reached at the end of the second phase and the final state, at the end of the third phase. In the equations below, V_t is the sample bulk volume given by the laser robot.

$$\phi_1 = 1 - \frac{V_1}{V_t} - \frac{(P_2 - P_3)V_2}{(P_1 - P_3)V_t} \tag{1}$$

$$\phi_2 = \frac{(P_{0+} - P_3)(V_t - V_1 - V_2)}{(P_1 - P_3)V_t} \tag{2}$$

The uncertainty on the pressure P_{0+} is high because of the thermal effects altering the pressure build-up at early times. Hence, ϕ is deduced from Equation (1) and P_{0+} is corrected using Equation (2) if required. In the KPC-Log technique, these effects are almost completely eliminated by filling the dead volume of the chamber V_1 as much as possible with calibrated billets and a powder. Among the various powders tested in the reference [19], we selected here talc. The intensity of the residual thermal effects can be assessed by comparing ϕ from Equation (2) to ϕ from Equation (1), *i.e.* ϕ_2 to ϕ_1. They are negligible when ϕ_2 is consistent with ϕ_1.

We chose a very small chamber V_2 for our KPC-Log device, to be in line with the device design advised in the reference [19]. When decreasing the expansion chamber capacity, the amplitude of the pressure build-up recorded outside the sample decreases, which can be prejudicial to the signal quality. At the same time, the amplitude of the pressure decay occurring inside the rock decreases. This is beneficial especially when Klinkenberg's method [20] is implemented to characterize the intrinsic permeability and the Klinkenberg coefficient. The need to work with a pressure variation in the porous medium remaining small compared to the mean pressure level is further discussed in Section 4.2. In conclusion, the volume of the chamber V_2 must be fixed by seeking a good compromise between the limitation of the pressure decay inside the sample and the quality of the pressure build-up outside the sample.

4. Interpretation

4.1. Numerical method for k_{app} estimation

4.1.1. 3D mesh

The numerical interpretation of a given KPC-Log test is divided into two phases. In the first phase, a 3D mesh of the whole system is constructed to enable the simulation of the gas flow from inside to outside the rock. The total volume around the sample, dead volume in the chamber V_1 added to the volume of the chamber V_2, is noted V_{1+2}. In the second phase, the apparent permeability k_{app} in our numerical model is adjusted by means of an optimization process, until matching the experimental pressure signal $P_{exp}(t)$ with the numerical one $P_{num}(t)$.

The whole system is meshed in several steps. To start with, a surface reconstruction algorithm is applied to the point cloud from the laser robot. Several algorithms exist and specific libraries allow easy access to some of them, as Computational Geometry Algorithms Library (CGAL) for example. The algorithm we drew from CGAL relies on Delaunay's 3D triangulation. It creates the point cloud convex envelope via a triangulation based on tetrahedra and eliminates the tetrahedra considered to be out of the porous medium. For information, we do not know if the laser robot uses the same algorithm, as its data processing program was totally developed by the manufacturer. The volume delimited by the envelope is meshed afterwards with regular hexahedra forming a cartesian grid. A mesh involving tetrahedra would be more relevant to faithfully reproduce the surface reconstructed earlier. However, an unstructured mesh is complex to handle for a simulator. Flux computation is seldom robust and accurate with an unstructured mesh and, when it is satisfactory, it is much more time-consuming than with a structured mesh. As a consequence, the structured mesh we build with regular hexahedra makes numerical calculations easier and faster but mars surface reproduction. The discrepancy between the bulk volume V_t' obtained from the cartesian grid and the reference V_t coming from the robot is sometimes not negligible. It can reach a few percents for the coarse grid used in the optimization process. This is the reason why the numerical porosity ϕ' assigned to the grid cells is not the experimental porosity ϕ computed from Equation (1) or Equation (2). Its value, determined from Equation (3), ensures the preservation of the true pore volume. Even if the type of mesh we chose is not ideal for an accurate 3D reconstruction, the results of Section 5 confirm that it is adequate for our application.

$$\phi' = \frac{\phi V_t}{V_t{}'} \tag{3}$$

The mesh generated for the sample is finally extended to the volume where the pressure build-up occurs. Its value V_{1+2} must be perfectly respected but its geometry has no impact on the simulation, the pressure outside the sample being supposed to be homogeneous. Hexahedra are piled all around the sample to define a parallelepipedic domain of volume V_{1+2}' close to V_{1+2}. The cell size is uniform in the whole grid and the domain edges do not cross or even touch the sample. Besides, the volume V_{1+2}' is corrected

by associating a porosity ϕ_{1+2}'$\neq$1 to the domain. Its value is deduced from Equation (4).

$$\phi_{1+2}' = \frac{V_{1+2}}{V_{1+2}{}'} \tag{4}$$

The algorithm we wrote for constructing the 3D mesh works for multiple pieces of rock as well. It meshes each piece from the related point cloud and then concatenates the grids by creating around them the grid corresponding to the volume V_{1+2}. Contact between either two pieces or one piece and the domain edges is avoided. The cell size is identical for all pieces and the volume V_{1+2}.

4.1.2. Numerical model

Our model describing the gas flow in the porous medium is based on the mass conservation equation and Darcy's law, given by Equation (5) and Equation (6) respectively.

$$\phi \frac{\partial \rho}{\partial t} + \nabla.(\rho \mathbf{v}) = 0 \tag{5}$$

$$\mathbf{v} = -\frac{k_{app}}{\mu} \nabla P \tag{6}$$

Concerning the notations, $\mathbf{v}$ is the gas velocity, ρ the gas density and μ the gas viscosity. The gas flow is supposed to be isothermal. As a result, ρ depends on P only and μ can be assimilated to a constant, the variation of μ with P being small in our tests. Moreover, the gas we opted for, nitrogen, authorizes the assumption of a perfect gas. We have implicitly made this assumption yet when deriving Equation (1) and Equation (2) from Boyle and Mariotte's law.

The gas flow outside the sample is also governed by Equation (5) and Equation (6) since the volume V_{1+2} acts as a porous medium in the simulation. The permeability in the grid cells of the domain surrounding the sample is very high, in order that the pressure equilibrates instantly in V_{1+2}' at any time. Notably, the permeability in V_{1+2}' is about 10^6 times higher than the rock permeability, in our simulations.

The gas velocity in the grid cells forming the domain edges is equal to 0, the walls of the chambers V_1 and V_2 being impermeable to gas. The simulation is initiated by fixing P to P_1 in the grid cells of the sample and P to P_{0+} in the grid cells around it.

4.1.3. Optimization process

The optimum k_{app} value is the solution of a minimization problem.

$$k_{app} = \underset{k_L < k_{app}{}^* < k_U}{argmin} \left(F(k_{app}{}^*) \right) \tag{7}$$

The function to be minimized is the objective function F, whose argument $k_{app}{}^*$ varies in the interval $[k_L - k_U]$.

$$F\left(k_{app}{}^*\right) = \int_0^{t_f} \left|P_{exp}(t) - P_{num}\left(t, k_{app}{}^*\right)\right| dt \qquad (8)$$

In Equation (8) defining F, t_f is the final time of the test. The integral is estimated numerically for each new $k_{app}{}^*$ value, *i.e.* at the end of each iteration of the optimization process. Any grid cell around the sample can be selected to obtain the P_{num} values at the end of the simulation time steps. Both P_{exp} and P_{num} are considered to be piecewise linear functions. This means that the computation of any missing pressure value, at an experimental time for P_{num} or at the end of a simulation time step for P_{exp}, is done by linear interpolation. The minimization problem is solved thanks to a classic gradient descent algorithm.

In order to speed up the convergence towards the best k_{app} value, our optimization process works in two times. A first little time-consuming run with a coarse grid gives a rough k_{app} value, noted $k_{app,c}$, acting as initial guess in a second run with a fine grid. In most cases, the number of simulations needed during the second run to find a more accurate k_{app} value, noted $k_{app,f}$, is small owing to the fact that $k_{app,c}$ is close to $k_{app,f}$. Time saving can be substantial since decreasing cell size makes simulation time increase quickly. The coarse grid involves a cell size higher than that of the fine grid by a factor of 2 to 4. In other words, the coarse grid includes 8 to 64 times fewer cells than the fine grid.

4.2. Klinkenberg's method for k_{abs} and b estimation

When gas is injected, the measured permeability is not a property intrinsic to the rock. It depends not only on the material but also on the gas nature and the gas pressure. The frequency at which fluid molecules collide with pore walls is higher for a gas than for a liquid. Consequently, the gas velocity at the pore walls is not equal to 0, which enhances the gas flow in the medium. This phenomenon, known as gas slippage effect, was first described in 1941 by Klinkenberg [20]. The author introduced Equation (9) correlating permeability to gas and permeability to liquid, k_{app} and k_{abs} respectively.

$$k_{app} = k_{abs}\left(1 + \frac{b}{P}\right) \qquad (9)$$

The permeability to liquid is considered to be absolute or intrinsic to the rock as it is exclusively controlled by the pore network structure. The permeability to gas is said to be apparent as it does not depend on the material only. It is also influenced by the gas pressure and the gas nature. The gas nature effect is hidden in the corrective factor b, named Klinkenberg coefficient.

Equation (9) is a local equation verified at any point of the sample. For an isothermal, 1D and steady-state gas flow, Equation (9) can be replaced by Equation (10) after integration along the sample [5].

$$\langle k_{app}\rangle = k_{abs}\left(1 + \frac{b}{\langle P\rangle}\right) \qquad (10)$$

At the macroscopic scale, the gas flow at the mean pore pressure <P> is driven by a mean apparent permeability

<k_{app}>. Equation (10) is behind the method proposed by Klinkenberg to determine k_{abs} and b from several steady-state tests executed at increasing <P>. The <k_{app}> values resulting from the interpretation of the different tests are plotted against 1/<P>. The properties k_{abs} and b are then deduced from the coefficients of the regression line over the data points. For more simplicity in the notations, the brackets < > added around k_{app} to designate the property at macroscopic scale will be subsequently omitted (as in Section 4.1.3).

Inversing numerically the pressure response recorded during a GRI-type test is not appropriate to characterize k_{abs} and b simultaneously. Profice *et al.* [21] proved that these properties are correlated, which means that a good match between the experimental signal and the numerical one is achieved for several pairs (k_{abs}, b). Klinkenberg's method provides reliable k_{abs} and b estimations if <P> is properly defined or controlled, as explained below. In the opposite case, it leads to erroneous estimations. All these elements likely justify why k_{app} values are preferentially delivered by commercial laboratories [15].

For a core plug subjected to a steady-state test, <P> is the average of the pressures at the inlet and outlet faces. A GRI-type test occurs at unsteady-state from beginning to end. In such a purely transient test, what is <P>? Total and I2M-TREFLE laboratory focused on this question in a study jointly conducted on the GRI technique [21, 22]. For a monodisperse pack of homogeneous and isotropic spheres undergoing a GRI test at a regulated temperature (refer to Figure 2), Equation (11) predicts the pressure at the surface of the particles over time. In this equation, R is the mean particle radius, C the gas compressibility and γ_i the ith root of Equation (14). The initial-boundary value problem was linearized by supposing that C is constant, to enable the computation of an analytical solution.

$$P(R,t) = \left[\alpha + \sum_{i=1}^{\infty} \beta_i e^{-\frac{\gamma_i^2 k_{app}}{\phi\mu R^2 C}t}\right]^{1/2} \qquad (11)$$

$$\alpha = P_2{}^2 + \frac{P_{0+}{}^2 - P_2{}^2}{1 + \frac{V_p}{V_{1+2}}} \qquad (12)$$

$$\beta_i = \frac{\left(P_{0+}{}^2 - P_2{}^2\right)\sin\gamma_i}{\frac{\gamma_i\cos\gamma_i}{2} + \left(1 + \frac{3V_p}{2V_{1+2}}\right)\sin\gamma_i} \qquad (13)$$

$$\tan\gamma_i = \frac{\gamma_i}{1 + \frac{\gamma_i^2 V_{1+2}}{3V_p}} \qquad (14)$$

It is interesting to emphasize that the compressibility of a perfect gas is equal to 1/P. The assumption consisting in assimilating 1/<P> to C was tested numerically. Several direct simulations of GRI tests were first run for different pressure excitations, with a numerical model considering gas slippage and gas compressibility variation over time. The signal from each direct simulation was then inverted twice. In the first inverse simulation, k_{app} was determined by using the direct simulation model with b=0 to ignore

gas slippage. In the following one, C was obtained from Equation (11) and the k_{app} value previously estimated. To finish, k_{app} was plotted against C and the couple (k_{abs}, b) resulting from the linear regression was compared to that acting as input in the direct simulations. With $<P>=1/C$, the errors on k_{abs} and b were small. With $<P>=<P(R,t)>$, $<P(R,t)>$ being the average pressure at the surface of the particles, they were systematically higher.

The reason why C is a good approximation of $1/<P>$ is still unclear. However, the common practice consisting in defining $<P>$ as $<P(R,t)>$ is undeniably wrong and this is obvious when having two things in mind. First, $<P>$ is the mean pore pressure in a steady-state test. Second, in a standard GRI test, $<P(R,t)>$ cannot be close to $<P(0,t)>$, mean pressure at the centre of the particles, since $P(R,t)$ and $P(0,t)$ vary in very different ranges. Generally, $P(R,t)$ decreases from P_{0+} by a few tens of millibars, V_{1+2} being large compared to V_p, whereas $P(0,t)$ increases by a few bars, V_p being initially at atmospheric pressure [15]. As a conclusion, the easiest way to overcome the problem due to $<P>$ characterization is to limit the pressure variation inside and outside the particles. In this case, $<P>$ can be effectively taken equal to $<P(R,t)>$ without affecting k_{abs} and b. The impact on k_{abs} and b of the value given to $<P>$ depending on the test design is illustrated in Section 5.2.

5. Experimental results

5.1. Materials

The rock we chose to validate the KPC-Log method was pyrophyllite, which is a low-grade metamorphic outcrop rock. Its name comes from its mineralogical composition including exclusively pyrophyllite minerals. Its absolute permeability does not exceed a few tens of nanodarcies. Besides, its ideal properties make it a good candidate to test methods adapted to low-permeability measurement: high homogeneity, low anisotropy and low sensitivity to mechanical stress and ambient humidity.

We took four plugs from our pyrophyllite block. All of them had a diameter of 23 mm and a length of 25 mm. One plug was sampled in each space direction, numbered from 1 to 3, to orientate and quantify anisotropy. The last plug was taken far from the others to check homogeneity. For each plug, we determined the k_{abs}, b and ϕ properties by Step Decay method [23]. The test consists in emitting several pressure pulses with nitrogen at the plug inlet and inversing the signal recorded at the outlet to estimate the three properties simultaneously. The effective confining pressure was set at 80 barg for the different tests. We did not clean the plugs to prevent rock damage. Drying was unnecessary since pyrophyllite permeability is quite not altered by ambient humidity. The results are presented in Table 1.

Table 1. k_{abs}, b and ϕ values for the pyrophyllite plugs

Plug	Direction	k_{abs} (nD)	b (bara)	ϕ (frac)
1	1	55	31	0.042
2	2	28	31	0.041
3	3	58	30	0.033
4	1	61	29	0.042

The results corroborate that pyrophyllite is homogeneous and slightly anisotropic, the anisotropy ratio being equal to 2. The lowest k_{abs} value is observed in Direction 2 and in the plane perpendicular to that direction, k_{abs} is almost uniform.

After validation of the technique, we selected a shale rock for an application case. This shale was that we used in the reference [15] to analyze GRI methods available in the industry. Its properties are reported in Table 2. While ϕ was deduced from a simple pycnometry test on a core plug (23*24 mm), k_{abs} and b were measured on different samples and with different methods. Darcypress tests [5] were done on small cylinder-shaped samples (10*5 mm), oriented parallel and perpendicular to bedding to evaluate anisotropy. They were followed by Darcyshale tests [19] on crushed rock (average particle diameter of 1.72 mm). The axial confining pressure was fixed to 100 barg in all Darcypress tests. We did not clean the sample. We only dried them in an oven at 65 °C until mass stabilization to eliminate the mobile liquids which could have generated biases in the measurements. The initial liquid phase was probably not entirely eliminated at 65 °C. However, this is not problematic since our goal was not to find a "true" permeability but to control the consistency of the results coming from various methods.

Table 2. k_{abs}, b and ϕ values for the shale samples

| Cylinder - 10*5 mm - // to bedding		Cylinder 23*24 mm
k_{abs} (nD)	b (bara)	
28	18	ϕ (frac)
Cylinder - 10*5 mm - ⊥ to bedding		
k_{abs} (nD)	b (bara)	
8	28	0.141
Crushed sample - 1.72 mm		
k_{abs} (nD)	b (bara)	
10	33	

5.2. Method validation

The pyrophyllite samples used to validate the KPC-Log method can be seen in the photos of Figure 7. A cylinder having a diameter of 38 mm and a length of 50 mm was taken in Direction 2 and cut in two half-cylinders with a saw. One half-cylinder was damaged with a hammer and a chisel. Neither the cylinder nor the half-cylinders were cleaned or dried.
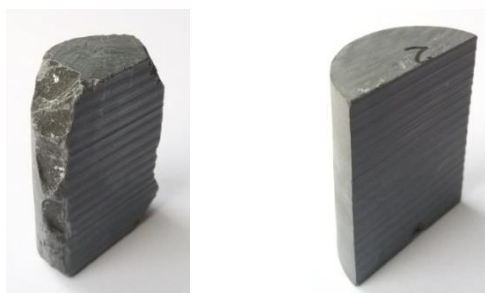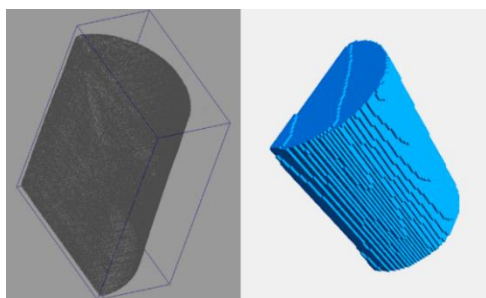
a. Broken half-cylinder   b. Intact half-cylinder

Fig. 7. Pyrophyllite half-cylinders

Standard GRI tests (refer to Figure 2) were carried out on the cylinder before cutting it along the longitudinal axis. The pressure P_1 in the chamber V_1 successively reached 4.2 bara, 6.9 bara and 9.9 bara. The chamber V_2 holding the cylinder was initially at atmospheric pressure in each test. KPC-Log tests were first done on the damaged half-cylinder only (refer to Figure 6). To assess the technique repeatability, some of them were reiterated in conditions as similar as possible. Nine tests were performed in total. The pressure P_1 in the chamber V_1 and the medium pore volume V_p ranged from 10.8 bara to 52.8 bara, each test beginning with the chamber V_2 at atmospheric pressure. To validate the code written for multiple pieces of rock, three KPC-Log tests were then undertaken on both half-cylinders put together in the chamber V_1. The pressure P_1 was set at 26.5 bara, 31.3 bara and 42.4 bara. Each series of GRI or KPC-Log tests was interpreted by applying the whole procedure detailed in Section 4, from the 3D mesh generation to k_{abs} and b characterization. Figure 8 shows, for both half-cylinders, the 3D point cloud coming from the laser robot and the resulting 3D cartesian grid.
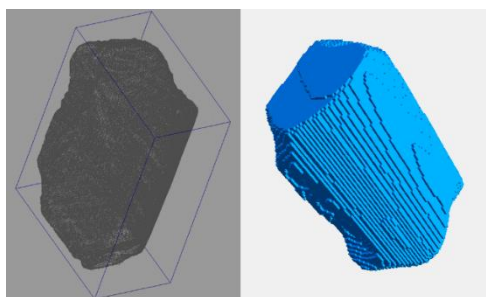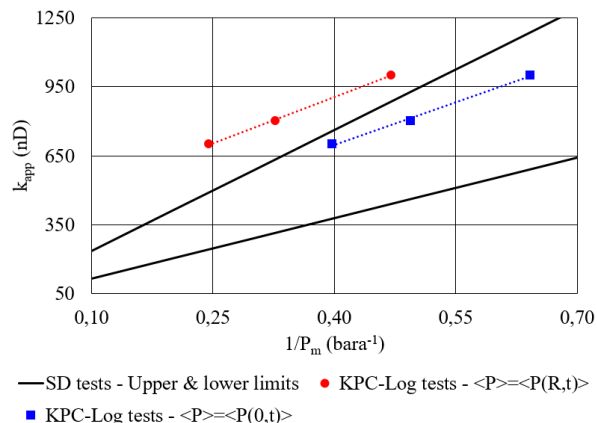
a. Broken half-cylinder
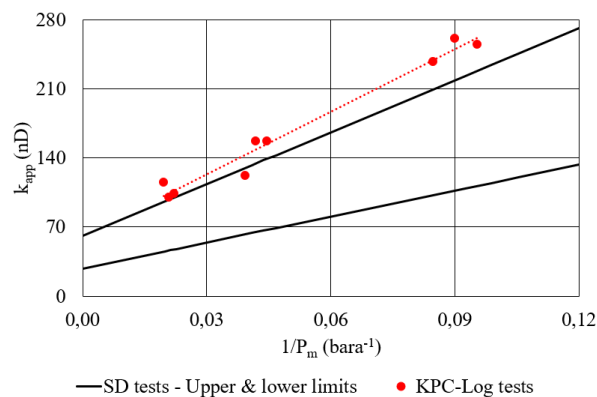
b. Intact half-cylinder

Fig. 8. 3D point clouds and cartesian grids for the pyrophyllite half-cylinders

For the cylinder, the linear regression leading to k_{abs} and b was accomplished twice, first with $<P>=<P(R,t)>$ and second with $<P>=<P(0,t)>$. The graphs of Figure 9.a, Figure 9.b and Figure 9.c give k_{app} plotted against $1/<P>$ for the cylinder, the damaged half-cylinder and both half-cylinders respectively. In all graphs, two lines demarcate the area where the $(1/<P>, k_{app})$ points are expected to be located. They were drawn considering Equation (10), *i.e.* Klinkenberg's law, and the data listed in Table 1: k_{abs} and b values in Direction 2 for the lower limit line, mean k_{abs}
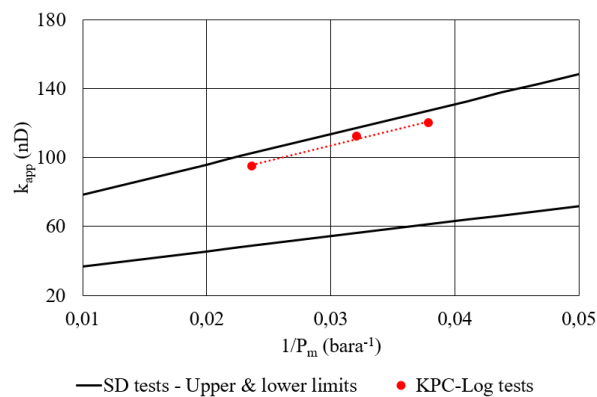
and b values in the plane perpendicular to Direction 2 for the upper limit line. In Table 3 are reported the k_{abs} and b values determined from the coefficients of the regression lines plotted in the graphs.

a. Cylinder

b. Broken half-cylinder

c. Broken half-cylinder and intact half-cylinder

**Fig. 9.** Graphs of k_{app} plotted against $1/<P>$ for the pyrophyllite samples

Table 3. k_{abs} and b values for the pyrophyllite samples

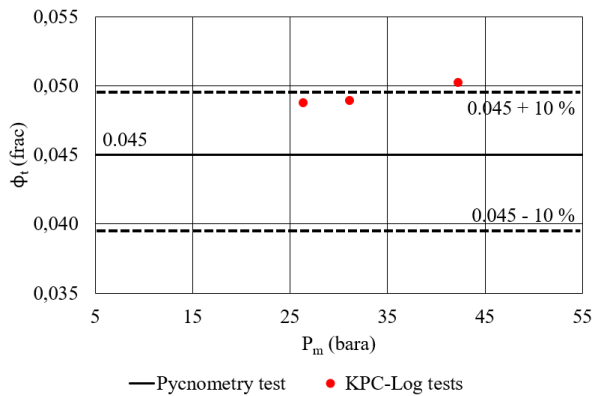| Cylinder			
$<P>=<P(R,t)>$		$<P>=<P(0,t)>$	
k_{abs} (nD)	b (bara)	k_{abs} (nD)	b (bara)
368	4	202	6
Broken half-cylinder			
k_{abs} (nD)		b (bara)	
60		35	

Broken half-cylinder and intact half-cylinder	
k_{abs} (nD)	b (bara)
54	33

Each half-cylinder underwent a pycnometry test with Micromeritics' Accupyc II 1340 device, which works as our KPC-Log device except that helium is injected. The goal was to associate a reference porosity, delivered by a device different from the KPC-Log device, to the broken half-cylinder on one hand and the set of half-cylinders on the other hand. This reference is simply ϕ_1 deduced from Equation (1) and the helium pycnometry data. A ϕ_2 value was derived from Equation (2) after each KPC-Log test. The diverse ϕ_2 values are compared to ϕ_1 in the graph of Figure 10.a for the broken half-cylinder and in the graph of Figure 10.b for the set of half-cylinders.
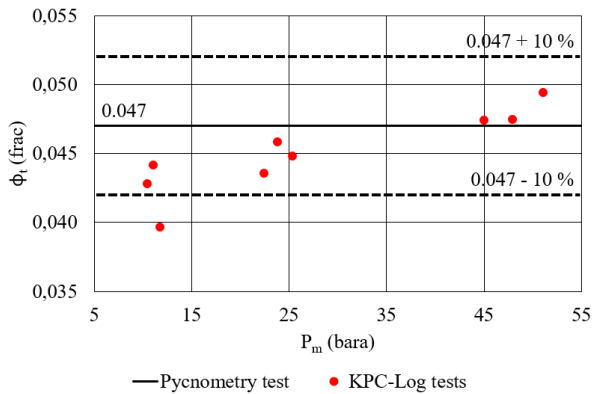
a. Broken half-cylinder

b. Broken half-cylinder and intact half-cylinder

Fig. 10. Graphs comparing the ϕ_2 values to the ϕ_1 value for the pyrophyllite samples

The impact of the pyrophyllite anisotropy on the gas flow was minimized by plugging parallel to Direction 2 the cylinder at the origin of the half-cylinders. The rock properties are indeed virtually homogeneous in the plane perpendicular to Direction 2. For both series of KPC-Log tests, the (1/<P>, k_{app}) points are well aligned, practically along the upper limit line. This observation is consistent with the fact that the gas propagation is mainly driven by the average properties along Direction 1 and Direction 3, the upper limit line being based on these properties. The errors on k_{abs} and b reach 6 % and 18 % respectively for the broken half-cylinder. They are even more negligible for the set of half-cylinders since, for it, they are equal to

4 % and 8 % respectively. For the series of GRI tests, the line formed by the (1/<P>, k_{app}) points does not diverge so much from the upper limit line, no matter how <P> is defined. Nevertheless, the biases affecting k_{abs} and b are significant in both cases. As an example, in the best case where <P>=<P(0,t)>, k_{abs} is overestimated by a factor of 3.6 while b is underestimated by a factor 5.1. These last results back the fact that P(0,t) variation must be limited during the test in order that accurate k_{abs} and b values can be found. To finish, the good consistency between the ϕ_1 and ϕ_2 values for both media studied with the KPC-Log technique highlights that the talc powder was efficient to reduce the thermal effects at short times.

The pressure signals coming from the tests on the set of half-cylinders were inverted twice, with the KPC-Log code and with Cydar software developed by Cydarex for the interpretation of laboratory petrophysical tests. In this software, we used the module specific to PDOS tests [5] (refer to Section 1), in order to appraise how simplifying the sample geometry impacts k_{abs} and b. We built a basic model in which all volumes characterizing the KPC-Log device (chambers and powder) were divided by 2 and the sample was either a sphere or a cylinder having the mean volume of one half-cylinder. We defined two geometries for the cylinder based on the average dimensions of one half-cylinder, being 1.9 cm for the radius and 5.0 cm for the length. In a first time, the cylinder diameter was fixed to 1.9 cm and its length was computed accordingly. In a second time, the cylinder length was fixed to 5.0 cm and its diameter computed. The k_{abs} and b values delivered by Cydar for the sphere and the cylinders are in Table 4.

Table 4. k_{abs} and b values for the sphere and the cylinders

Sphere - 3.7 cm	
k_{abs} (nD)	b (bara)
44	108
Cylinder - 1.9*9.4 cm	
k_{abs} (nD)	b (bara)
20	111
Cylinder - 2.6*5.0 cm	
k_{abs} (nD)	b (bara)
28	132

The results from the simulations involving the simplified geometries were compared to those from the simulations relying on the true geometry (refer to Table 3). It seems that simplifying the geometry has a more negative effect on b than on k_{abs}. Indeed, while k_{abs} is underestimated by a factor of 1.3 to 2.7, b is overestimated by a factor of 3.6 to 4.4.

5.3. Method application

We prepared a set of thirteen cube-shaped pieces of shale having dimensions of a few millimetres. Their forms and sizes were irregular since they were cut manually, with a simple saw. Our goal was to produce an artificial crushed sample comprising particles which are big enough so that their surfaces can be properly mapped by the laser robot. Some of these particles appear in the photo of Figure 11

and the concatenated 3D meshes of the thirteen particles can be observed in Figure 12.

Fig. 11. Cube-shaped particles of shale

Fig. 12. 3D cartesian grids for the particles of shale

The particles were not cleaned but dried at 65 °C before scanning with the robot. We conducted on them a series of tests with the Darcyshale device. The KPC-Log device was inappropriate because of its chamber V_1 designed for big samples only. The recorded pressure build-ups were interpreted twice, first using Cydar and second using the numerical model working with the true sample geometry. The particles were represented by spheres in Cydar. The (k_{abs}, b) pairs coming from both interpretations are listed in Table 5 and their corresponding (1/<P>, k_{app}) datasets are compared to those from reference [15] in the graph of Figure 13.

Table 5. k_{abs} and b values for the particles of shale

True sample geometry	
k_{abs} (nD)	b (bara)
25	21
Simplified sample geometry	
k_{abs} (nD)	b (bara)
25	38

—— Horizontal cylinder (10*5 mm) - Darcypress

---- Vertical cylinder (10*5 mm) - Darcypress

● Crushed sample - Darcyshale - Simplified geometry (spheres)

● Cube-shaped particles - Darcyshale - Simplified geometry (spheres)
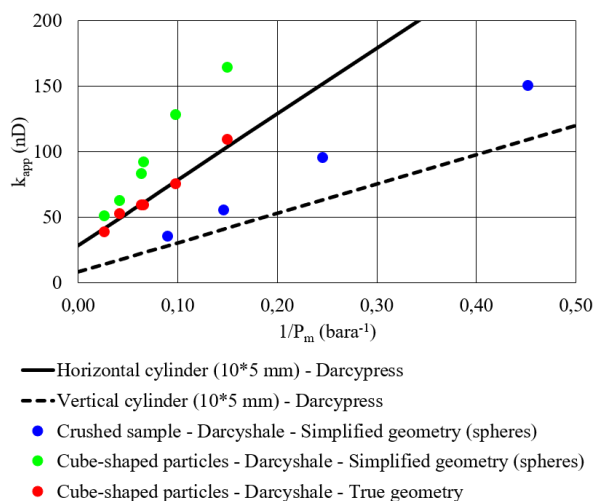
● Cube-shaped particles - Darcyshale - True geometry

Fig. 13. Graph comparing both (1/<P>, k_{app}) datasets related to the particles of shale to datasets from the reference [15]

The discrepancy between the k_{abs} values is quite equal to 0 and that between the b values is less than a factor of 2.

As already highlighted in Section 5.2, b is more sensitive than k_{abs} to the geometry. When accurately capturing the shapes of the particles, the (1/<P>, k_{app}) points are more consistent with those from past experiments described in the reference [15], especially at low pressures where b is meaningful. The influence of the geometry on k_{abs} and b remains yet negligible in this specific case. This suggests that our cube-shaped particles of shale can be reasonably modelled by spheres. As the numerical results detailed in the reference [17], our experimental results confirm that cuttings or crushed rock particles can be supposed to be spherical if they are not excessively elongated.

6. Summary and conclusions

This paper focuses on the KPC-Log method designed for characterizing the properties of a tight sample having any shape, a geometrical one or not. Each test is an improved GRI test resting upon the experimental recommendations formulated in the reference [19] and leading to k_{app} and ϕ values. The recorded signal is a pressure build-up due to gas expansion from inside to outside the porous medium. By pressurizing the material and limiting the surrounding volume, the pressure variation in the pore volume is kept small during the test. This is crucial when estimating k_{abs} and b from a series of tests at increasing pore pressures, by applying Klinkenberg's method. Indeed, <P>, whose definition is not trivial in a purely unsteady-state test, is correctly approximated by the value of the mean pressure level. This is not true when the pore volume experiences huge pressure variations. Consequently, reliable k_{abs} and b values are found from the coefficients of the regression line over the (1/<P>, k_{app}) points. The KPC-Log method relies on another key element, namely the introduction of a powder in the dead volume of the chamber containing the sample. The talc used in the tests proved to decrease efficiently the thermal effects occurring at short times. A test is interpreted with a numerical model and a 3D mesh of the system composed of the chambers and the sample. The mesh is created from a 3D point cloud of the sample surface that a robot captures by laser mapping. The code producing the mesh was initially written for one piece of rock. It was extended afterwards for several pieces, each piece having its own point cloud.

We validated our technique on pyrophyllite, an ideal low-permeability material having known properties. We successively used one big half-cylinder and a set of two half-cylinders. Afterwards, we implemented the method on a pack of small cube-shaped particles of shale. From each series of tests were estimated k_{abs} and b values with an accurate reconstruction of the sample and a simplified one as well. The goal was to appraise how k_{abs} and b are affected when the true sample geometry is not respected. The results demonstrated that the error on b arising from geometry simplification systematically exceeds the error on k_{abs}. This means that the error on k_{app} increases when the pressure decreases. Besides, the experimental results from the tests on the small particles of shale corroborated one conclusion drawn from the numerical study detailed in the reference [17]. Modelling cuttings or crushed rock

particles by spheres is adequate if their shapes are not too elongated.

The k_{abs} and b values coming from KPC-Log tests are more accurate than those from standard GRI tests. They are also more representative since crushing can engender microfractures and distort the pore network. Keeping the material intact has for other notable advantage to enlarge the range of measurable permeabilities, the signals being longer owing to the larger distances traveled by the gas. The KPC-Log method offers a new option to build a log of permeability along the well if a MCB is preferred for drilling, given that this tool delivers centimetric pieces of rock at the surface. Moreover, even if the technique was initially developed for unconventional formations, its use could be extended to conventional ones by replacing gas with liquid [3]. Finally, additional improvements would be needed in the future to solve the remaining problems that the KPC-Log technique has still in common with the GRI technique: sample anisotropy, sample fracturing and no sample confinement.

References

1. C. E. Molinares, R. M. Slatt and R. Sierra, "The effects of lamination/bedding on the brittleness for the Woodford shale silica-rich intervals, from the Wyche-1 core-well analysis, Pontotoc County, Oklahoma", presented at the AAPG Annu. Conv. and Exhib., Houston, TX, USA, Apr. 2 - 5, 2017.

2. D. L. Luffel, C. W. Hopkins and P. D. Shettler, "Matrix permeability measurement of gas productive shales", presented at the SPE Annu. Tech. Conf. and Exhib., Houston, TX, USA, Oct. 3 - 6, 1993, Paper SPE 26633.

3. P. Egermann, R. Lenormand, D. Longeron and C. Zarcone, "A fast and direct method of permeability measurement on drill cuttings", *Petrophysics*, vol. 44, n° 4, pp. 243 - 252, Jul. - Aug. 2003, doi: 10.2118/77563-PA.

4. P. Carles, P. Egermann, R. Lenormand and J.-M. Lombard, "Low permeability measurements using steady-state and transient methods", presented at the SCA Int. Symp., Calgary, AB, Canada, Sep. 10 - 12, 2007, Paper SCA2007-07.

5. R. Lenormand, F. Bauget and G. Ringot, "Permeability measurement on small rock samples", presented at the SCA Int. Symp., Halifax, NS, Canada, Oct. 4 - 7, 2010, Paper SCA2010-A073.

6. X. Cui, A. M. M. Bustin and R. M. Bustin, "Measurements of gas permeability and diffusivity of tight reservoir rocks: different approaches and their applications", *Geofluids*, vol. 9, pp. 208 - 223, 2009, doi: 10.1111/j.1468-8123.2009.00244.x.

7. Y. Zhao, C. Wang and J. Bi, "A method for simultaneously determining axial permeability and transverse permeability of tight reservoir cores by canister degassing test", *Energy Sci. Eng.*, vol. 8, n° 4, pp. 1220 - 1230, Apr. 2020, doi: 10.1002/ese3.580.

8. M. J. Hannon Jr., "Fast and reliable estimates of low permeabilities by the Full-Immersion Pressure-Pulse Decay", presented at the SPE/AAPG/SEG Unconventional Resources Technol. Conf., Austin, TX, USA, Jul. 24 - 26, 2017, Paper URTeC: 2669302.

9. S. Peng and B. Loucks, "Permeability measurements in mudrocks using gas-expansion methods on plug and crushed-rock samples", *Mar. Petrol. Geol.*, vol. 73, pp. 299 - 310, May 2016, doi: 10.1016/j.marpetgeo.2016.02.025.

10. O. Kwon, A. K. Kronenberg, A. F. Gangi and B. Johnson, "Permeability of Wilcox shale and its effective pressure law", *J. Geophys. Res.-Atmos.*, vol. 106, n° B9, pp. 19,339 - 19,353, Sep. 10, 2001, doi: 10.1029/2001JB000273.

11. C. David, J. Wassermann and the KG²B team, "KG²B, a collaborative benchmarking exercise for estimating the permeability of the Grimsel granodiorite - Part 1: measurements, pressure dependence and pore-fluid effects", *Geophys. J. Int.*, vol. 215, n° 2, pp. 799 - 824, Nov. 1, 2018, doi: 10.1093/gji/ggy304.

12. S. Sinha, E. M. Braun, Q. R. Passey, S. A. Leonardi, A. C. Wood III, T. Zirkle, J. A. Boros and R. A. Kudva, "Advances in measurement standards and flow properties measurements for tight rocks such as shales", presented at the SPE/EAGE Eur. Unconventional Resources Conf. and Exhib., Vienna, Austria, Mar. 20 - 22, 2012, Paper SPE 152257.

13. A. Tinni, E. Fathi, R. Agarwal, C. Sondergeld, Y. Akkutlu and C. Rai, "Shale permeability measurements on plugs and crushed samples", presented at the SPE Can. Unconventional Resources Conf., Calgary, AB, Canada, Oct. 30 - Nov. 1, 2012, Paper SPE 162235.

14. J. T. Comisky, M. Santiago, B. McCollom, A. Buddhala and K. E. Newsham, "Sample size effects on the application of mercury injection capillary pressure for determining the storage capacity of tight gas and oil shales", presented at the SPE Can. Unconventional Resources Conf., Calgary, AB, Canada, Nov. 15 - 17, 2011, Paper CSUG/SPE 149432.

15. S. Profice and R. Lenormand, "Low permeability measurement on crushed rock: insights", presented at the SCA Int. Symp., Pau, France, Sep. 26 - 30, 2019, Paper SCA2019-016.

16. F. Civan, "Can gas permeability of fractured shale be determined accurately by testing core plugs, drill cuttings and crushed samples?", presented at the SPE/AAPG/SEG Unconventional Resources Technol. Conf., Austin, TX, USA, Jul. 24 - 26, 2017, Paper URTeC: 2666389.

17. R. Suarez-Rivera, M. Chertov, D. Willberg, S. Green and J. Keller, "Understanding permeability measurements in tight shales promotes enhanced determination of reservoir quality", presented at the

SPE Can. Unconventional Resources Conf., Calgary, AB, Canada, Oct. 30 - Nov. 1, 2012, Paper SPE 162816.

18. S. Desmette, B. Deschamps, R. Birch, M. Naegel and P. Essel, "Drilling hard and abrasive rock efficiently or generating quality cuttings? You no longer have to choose…", presented at the SPE Annu. Tech. Conf. and Exhib., Denver, CO, USA, Sep. 21 - 24, 2008, Paper SPE 116554.

19. R. Lenormand and S. Profice, "Darcyshale: an improved GRI method for more reliable measurements on low-permeability samples", presented at the SCA Int. Symp., Austin, TX, USA, Sep., 2021, Paper SCA2021-T040.

20. L. J. Klinkenberg, "The permeability of porous media to liquids and gases", in *Drilling and Production Practice*. New-York, NY, USA: API, 1941, pp. 200 - 213.

21. S. Profice, D. Lasseux, Y. Jannot, N. Jebara and G. Hamon, "Permeability, porosity and Klinkenberg coefficient determination on crushed porous media", presented at the SCA Int. Symp., Austin, TX, USA, Sep. 18 - 21, 2011, Paper SCA2011-32.

22. S. Profice, "Mesure de propriétés monophasiques de milieux poreux peu perméables par voie instationnaire", Ph.D. dissertation, I2M - Dept. TREFLE, Bordeaux Univ., Bordeaux, France, 2014.

23. D. Lasseux, Y. Jannot, S. Profice, M. Mallet and G. Hamon, "The "Step Decay": a new transient method for the simultaneous determination of intrinsic permeability, Klinkenberg coefficient and porosity on very tight rocks", presented at the SCA Int. Symp., Aberdeen, Scotland, Aug. 27 - 30, 2012, Paper SCA2012-25.

Nomenclature

b (Pa)	Klinkenberg coefficient
C (Pa^{-1})	Gas compressibility
F	Objective function
k (m^2)	Permeability
P (Pa)	Pressure
R (m)	Mean particle radius
t (s)	Time
T (K)	Temperature
v (- / m.s^{-1})	Valve / Darcy gas velocity
V (m^3)	Volume
μ (Pa.s)	Gas viscosity
ρ (kg.m^{-3})	Gas density
ϕ (frac)	Porosity
$\langle \, . \, \rangle$	Mean property

Subscripts

abs	Absolute
app	Apparent
c	Coarse grid
exp	Experimental
f	Final / Fine grid
num	Numerical
p	Pore
t	Total
0+	Just after valve opening
1	Chamber 1 - Initial state (IS) Material balance between IS and FS
2	Chamber 2 - Transitional state (TS) Material balance between IS and TS
3	Final state (FS)
1-2	Between Chamber 1 and Chamber 2
1+2	Chamber 1 and Chamber 2 as a whole

Exponents

'	Cartesian grid